Available online at www.sciencedirect.com
SCIENCE DIRECT®
Journal of Catalysis 222 (2004) 152–166
JOURNAL OF CATALYSIS
www.elsevier.com/locate/jcat

Effects of morphology on surface hydroxyl concentration: a DFT comparison of anatase–TiO_2 and γ-alumina catalytic supports

C. Arrouvel,[a] M. Digne,[b,1] M. Breysse,[c] H. Toulhoat,[d] and P. Raybaud [a,*]

[a] *Direction Chimie et Physico-chimie Appliquées, Institut Français du Pétrole, 1-4 avenue de Bois-Préau, 92852 Rueil-Malmaison cedex, France*
[b] *Laboratoire de Chimie, UMR 5532, Ecole Normale Supérieure de Lyon, 46 allée d'Italie, 69364 Lyon cedex 07, France*
[c] *Laboratoire de Réactivité des Surfaces, UMR CNRS, Université Pierre et Marie Curie, 4 Place Jussieu, 75252 Paris cedex 05, France*
[d] *Direction scientifique, Institut Français du Pétrole, 1-4 avenue de Bois-Préau, 92852 Rueil-Malmaison cedex, France*

Received 11 July 2003; revised 6 October 2003; accepted 21 October 2003

Abstract

A comparative investigation of surface hydroxylation states for anatase–TiO_2 and γ-alumina is crucial for a better understanding of how these materials behave as catalytic supports under working conditions. Our approach combines density functional simulations and thermodynamic analysis, to determine the types of hydroxyls existing on the (100), (101), (001), and (110) surfaces of anatase–TiO_2, as a function of temperature and water pressure. The vibrational analysis of surface OH groups allows for the assignment of experimental infrared bands as a function of the surface orientation. A consistent and quantitative comparison with recent DFT simulations on γ-alumina highlights the different acidic–basic properties of the two supports. Finally, we suggest directions for increasing the density of basic and exchangeable hydroxyls which is governed by morphology effects.

Keywords: Anatase–TiO_2; γ-Alumina; Density functional theory (DFT); Surface property; Morphology; Nanoparticles; Hydroxyl groups; Brønsted acidity; Hydrotreatment; Infrared (IR)

1. Introduction

The environmental specifications for producing diesel with lower residual sulfur content prompt researchers to keep improving the activity of hydrodesulfurization catalysts. Since the industrial catalyst is made of a Co(Ni)MoS active phase dispersed over a γ-alumina support [1,2], the gain in activity can be reached by improving either the active phase or the support. Huge efforts have been undertaken for optimally tuning the textural and acidic properties of the γ-alumina support [3]. Besides the industrially used γ-alumina, numerous experimental studies have shown that a nonpromoted MoS_2 phase dispersed over anatase–TiO_2 exhibits a higher intrinsic catalytic activity than γ-alumina-supported MoS_2 [4,5]. Furthermore, novel methods of preparation, as reported recently by Dzwigaj et al. [6], seem to open new routes for producing high surface area anatase–TiO_2. However, the Co (or Ni)-promoting effect on the intrinsic activity is significantly less pronounced on anatase–TiO_2 than on γ-alumina [4,7]. Several proposals have been put forward to explain these experimental observations. Among them, the role of the support on the dispersion (number of active sites) and on the sulfurability of the active phase has been invoked together with electronic, geometrical, or orientation effects. However, up to now, no clear evidence has been given supporting an explanation of the different catalytic behaviors of alumina- and anatase-based catalysts.

As a first step in helping to answer these challenging questions, a better description of the surface acidic–basic properties of the support is needed in order to explore the further impact on the reactivity and interaction with the active phase. Many experimental works underlined the extent to which the particle sizes and shapes of anatase–TiO_2 powders may be modified upon various preparation conditions [8–14], thereby affecting the textural properties (surface area, pore-size distributions). Most commonly, the observed shapes exhibit the (101) and (001) surfaces, as characterized by HRTEM and XRD techniques. However, it seems to

* Corresponding author.
E-mail address: pascal.raybaud@ifp.fr (P. Raybaud).
[1] Current address: Direction Physique et Analyse; IFP-Lyon, BP No. 3-69390 Vernaison, France.

0021-9517/$ – see front matter
doi:10.1016/j.jcat.2003.10.016

be possible to observe other crystallographic planes [9,10]. At the same time, many relevant infrared (IR) spectroscopy studies attempted to determine the types of hydroxyl groups present at the surface of anatase particles [15–20]. These studies reveal the difficulties of assigning unambiguously the different types of OH groups. Numerous bands corresponding to OH species are observed by some IR experiments [15–17]. Some OH-stretching frequencies were observed between 3600 and 3800 cm^{-1} and 3350 and 3500 cm^{-1}, while OH groups involved in hydrogen bonds have a signature at about 3300 cm^{-1}. A strong band at 1620 cm^{-1} would also correspond to the bending mode of H_2O chemisorbed at the surface [16,17]. However, the type and number of OH groups revealed by IR depend on the sample origin as well as on the preparation conditions (temperature, water pressure) leading to different surface species or possibly to different morphologies.

Whereas many theoretical studies were devoted to the rutile phase of TiO_2, fewer investigations on the anatase phase [21], which is the stable phase under hydrotreating conditions, are available in the literature. Empirical approaches [22] and atomistic simulations [23] attempted to determine the morphology of anatase and found that the crystallites shape was a truncated bipyramid exposing the (101) and (001) surfaces. However, these methods do not take into account either the surface relaxation energies or the hydration energies, expected to play a key role in the stabilization of oxide surfaces. Semiempirical [24], Hartree-Fock [25], and DFT [26] simulations found that water adsorbs dissociatively on the (001) surface. Although these studies are useful for a first step toward a better understanding of the water–surface interaction, none has undertaken a systematic approach of the anatase surface hydration process, as a function of temperature and pressure. This effect may be crucial for a rigorous determination of the acidic–basic properties of anatase. Furthermore, no theoretical assignment of the IR bands has been attempted up to now.

Recent DFT calculations proved the efficiency of this method for determining surface energies and morphologies as a function of working conditions for the Co(Ni)MoS active phase [27,28], as well as for aluminum oxide systems [29,30]. In the same spirit, the goal of the present paper is to determine by DFT calculations the hydration state of four crystallographic planes of anatase–TiO_2 in wide ranges of temperature and water pressure (p_{H_2O}), including those prevailing under working conditions of hydrodesulfurization (HDS) reactions, further referred to as "hydrotreating conditions" (i.e., $600 < T < 700$ K and low p_{H_2O}/p_0, where p_0 is the standard vapor pressure). The influence of p_{H_2S} will be addressed in a forthcoming paper. We recently proposed an approach enabling the hydration state of γ-alumina surfaces to be determined [30]. Using the same definition of the chemical potential of water, we correlate the conditions imposed by the gas phase and the hydration rate of the anatase nanoparticle surfaces. This enables all the configurations of water adsorbed at the anatase surfaces to be investigated for various water coverages, and to calculate the surface energies for four main crystallographic orientations: (101), (001), (100), and (110). The equilibrium morphology is then deduced from the Gibbs–Curie–Wulff law. Furthermore, the different types of surface hydroxyl groups are characterized by calculating the vibrational stretching frequencies and compared to IR experiments. Finally, in the discussion, we propose a quantitative comparison of the results obtained on anatase–TiO_2 and those on γ-alumina surfaces as published recently by Digne et al. [30].

2. Methods

2.1. DFT calculations

Total energy calculations are performed within the density functional theory (DFT) and the generalized gradient approximation (GGA) of Perdew and Wang [31]. To solve the Kohn–Sham equations, we used the Vienna ab initio simulation package (VASP) [32–35]. VASP performs an iterative diagonalization of the Kohn–Sham Hamiltonian via unconstrained band-by-band minimization of the norm of the residual vector to each eigenstate and via optimized charge density mixing routines. The convergence criterion for the electronic self-consistent cycle is fixed at 0.1 meV per cell. The eigenstates of the electron wave functions are expanded on a plane–waves basis set using pseudopotentials to describe the electron–ion interactions within the projector augmented waves (PAW) approach [36]. For total energy calculations, we use a cutoff energy of 312.5 eV. The optimization of the atomic geometry (also called relaxation) at 0 K is performed by using a conjugate gradient algorithm, and by determining the exact Hellman–Feynman forces acting on the ions for each optimization step. A full relaxation of all atomic positions in the cell was performed until the convergence criterion on the energy (0.1 meV/cell) was reached.

The OH-stretching modes are calculated within a harmonic approximation. The Hessian matrix is calculated by the finite difference approach, with a moving step size of 0.005 Å around the equilibrium position. The coupling with the first outmost layer of the surface is considered. The anharmonicity corrections for OH stretching are performed by following the procedure proposed by Ugliengo et al. and as implemented in the ANHARM program [37,38]. The anharmonicity corrections calculated by this approach are about 71–73 cm^{-1}, depending on the type of hydroxyl groups.

2.2. Surface energy calculations

For a nanocrystallite of a given volume, the Gibbs–Curie–Wulff law [39] allows the morphology to be determined according to the following relationship,

$$\frac{\Gamma_{hkl}}{d_{hkl}} = \alpha \quad \forall h,\ k,\ l, \tag{1}$$

where Γ_{hkl} is the surface energy for the (hkl) orientation, d_{hkl} stands for the distance from the surface to the center of mass of the solid, and α is a real constant independent from h, k, l. The objective of the present work is to calculate Γ_{hkl} as a function of the working conditions fixed by temperature and water pressure which have a direct influence on the hydration state of the support. DFT calculations enable accurate determination of the value of Γ_{hkl} for many different oxides [29,30,40]. For that purpose, we use an approach similar to that proposed in [30] and based on the following expression of the surface energy (referenced to the bulk energy),

$$A_{hkl}\Gamma_{hkl} = G(\mathrm{surf}_{hkl} + n\mathrm{H_2O}) - G(\mathrm{bulk}) - n\mu_{\mathrm{H_2O}}, \quad (2)$$

where $G(\mathrm{surf}_{hkl} + n\mathrm{H_2O})$ is the Gibbs free energy of the surface (hkl) with n adsorbed water molecules and a surface area of A_{hkl}, $G(\mathrm{bulk})$ is the Gibbs free energy of the bulk normalized to the number of atoms used in the supercell of a hydrated TiO_2 surface, and $\mu_{\mathrm{H_2O}}$ stands for the chemical potential of water.

Neglecting for the condensed phase the variation of entropy and pV terms, as well as thermal variations of internal energies, the surface energy of the (hkl) facet can be expressed as

$$\Gamma_{hkl} = \Gamma^0_{hkl} + \theta_{hkl}(E_{\mathrm{ads}} + \Delta\mu_{\mathrm{H_2O}}), \quad (3)$$

where Γ^0_{hkl} stands for the surface energy of the dehydrated surface and is determined by the following relationship,

$$\Gamma^0_{hkl} = \frac{G(\mathrm{surf}_{hkl}) - G(\mathrm{bulk})}{A_{hkl}} \approx \frac{E_{0K}(\mathrm{surf}_{hkl}) - E_{0K}(\mathrm{bulk})}{A_{hkl}}, \quad (4)$$

and E_{ads} is the adsorption energy of n adsorbed water molecules averaged over n:

$$E_{\mathrm{ads}} = \frac{G(\mathrm{surf}_{hkl} + n\mathrm{H_2O}) - G(\mathrm{surf}_{hkl})}{n} \approx \frac{E_{0K}(\mathrm{surf}_{hkl} + n\mathrm{H_2O}) - E_{0K}(\mathrm{surf}_{hkl})}{n}. \quad (5)$$

$\Delta\mu_{\mathrm{H_2O}}$ represents the chemical potential of water referenced to the internal energy of the isolated water molecule ($e_{\mathrm{H_2O}}$):

$$\Delta\mu_{\mathrm{H_2O}} = h^0_{\mathrm{H_2O}} - Ts^0_{\mathrm{H_2O}} + RT\ln\left(\frac{p_{\mathrm{H_2O}}}{p_0}\right) - e_{\mathrm{H_2O}}. \quad (6)$$

It is crucial to point out that Eq. (3) takes into consideration the surface coverage of adsorbed water. This coverage is represented by the parameter θ_{hkl} which is equal to n/A_{hkl}. The hydroxyl coverage is twice as large as the value of θ_{hkl}. Thus, for a given θ_{hkl}, it is necessary to determine the most favorable adsorption configuration of the water molecules leading to the lowest adsorption energy (E_{ads}): chemisorbed with dissociation, chemisorbed without dissociation, or physisorbed. Once this configuration is found, θ_{hkl} is allowed to vary. For a given working condition in T and $p_{\mathrm{H_2O}}$, the lowest value of Γ_{hkl} gives the stable hydration state of the surface.

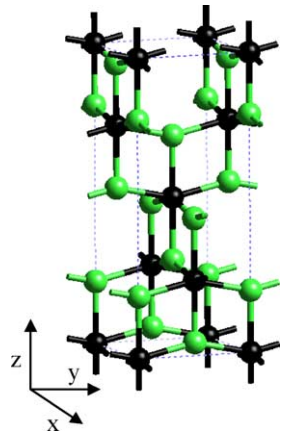

Fig. 1. Conventional cell of anatase TiO_2 (black balls, titanium atoms; gray balls, oxygen atoms).

3. Results

3.1. Bulk structure

In the following, the notations used for describing the various local ionic environments are μ_2-O (resp. μ_3-O) for two- (resp. three) fold coordinated oxygen atoms and Ti_{IV} (resp. Ti_V, Ti_{VI}) for tetra- (resp. penta-, hexa-) coordinated titanium atoms. The unsaturated Ti (resp. O) sites will be assimilated to Lewis acid (resp. basic) sites.

For the correct description of the conventional cell of the anatase bulk (see Fig. 1), we find that the convergence in energy is better than 10 meV/cell with respect to the k points grid when a $(6, 6, 6)$ mesh is used. The corresponding bulk energy will be used as the energy reference for all surface energy calculations (see Eq. (4)).

The conventional cell of the anatase phase contains 12 atoms, i.e., four TiO_2 units (see Fig. 1). Within the I41/amd space group, the tetragonal lattice symmetry gives a cell with $a_{\mathrm{exp}} = 3.776$ Å and $c_{\mathrm{exp}} = 9.486$ Å, and the resulting experimental volume $V_{\mathrm{exp}} = 135.25$ Å^3 [41,42]. The ionic experimental positions are fixed by the internal parameter, $w_{\mathrm{exp}} = 0.208$, defined as: $w = (d(\mathrm{Ti–O})_z)/c$. The optimized cell parameters are $a_{\mathrm{calc}} = 3.802$ Å, $c_{\mathrm{calc}} = 9.702$ Å, resulting in $V_{\mathrm{calc}} = 140.22$ Å^3 and $w_{\mathrm{calc}} = 0.207$, in good agreement with experimental data within the DFT-GGA-PAW accuracy. This optimized structure will be used for constructing slab models for surface simulations. In the bulk, oxygen atoms are tricoordinated (μ_3-O type) and titanium atoms are hexacoordinated (Ti_{VI} type) with a deformed octahedral environment. There exist two nonequivalent Ti–O distances: two $(\mathrm{Ti–O})_z$ bonds along the z axis, corresponding to 2.01 Å (exp 1.97 Å) and four shorter $(\mathrm{Ti–O})_{x,y}$ bonds belonging to the $(x\mathrm{O}y)$ plane, corresponding to 1.95 Å (exp

Table 1
Parameters used for the simulations of the TiO_2 bulk phase and (hkl) surfaces. ($\vec{u}$ is a linear combination of $\vec{a}$ and $\vec{b}$; $\vec{v}$ of $\vec{a}$ and $\vec{c}$)

	Bulk	hkl			
		001	100	110	101
Number of atoms	12	60	96	48	72
Number of layers	–	5	8	8	6
k points mesh	666	221	122	221	221
Surface periodicity	–	$2\vec{a}\times 2\vec{b}$	$2\vec{b}\times\vec{c}$	$\vec{v}\times\vec{c}$	$\vec{u}\times 2\vec{b}$
Vacuum thickness (Å)	–	9.7	12.7	10.0	14.1
Slab thickness (Å)	–	9.7	13.3	9.4	7.9
Surface areas (Å^2)	–	57.8	73.7	52.1	79.2

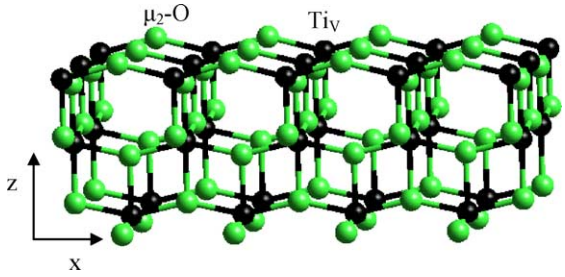

Fig. 2. Structure of the dehydrated (001) surface after relaxation ($\theta_{001}=0$) (same legend as Fig. 1).

1.93 Å). The shortest O–O distance is 2.48 Å (exp 2.46 Å) while the Ti–Ti distance is 3.08 Å (exp 3.03 Å).

3.2. Structure and energetics of the dehydrated surface

The optimized parameters used for the simulations are reported in Table 1 for the four crystallographic orientations: (001), (100), (110), and (101). For each surface, the k points grid, the *vacuum* thickness added to separate each neighboring slab, and the slab thickness (i.e., number of atomic layers) are carefully optimized to avoid electronic interactions between two slabs belonging to neighboring cells or between the two sides of the slab. In order to simulate various water coverages with a relevant number of sites and to allow sufficient degrees of freedom for surface reconstructions, rather large surface areas are chosen. For each surface orientation, a full slab relaxation is carried out by keeping constant the cell parameters. The crystal cleavage induces strong perturbations on the surface depending on the crystallographic orientation. The atoms on the surface become undercoordinated and, thus, undergo a local reorganization, which can propagate inside the slab. For oxides, it is well known that such a propagation can occur along many atomic layers requiring large slab thicknesses to be used.

3.2.1. (001) surface

The dehydrated (001) surface exhibits unsaturated Ti_V sites as well as μ_2-O and μ_3-O sites (see Fig. 2 and Table 2). The number of broken Ti–O bonds is 23.0 μmol m^{-2}, revealing quite a high degree of unsaturation. A reasonable number of layers (5) is sufficient for accurately describing the

Table 2
Surface concentrations (in μmol m^{-2}) of the different basic and acid Lewis sites for the dehydrated surfaces

	hkl			
	001	100	110	101
Ti_{VI}	–	9.0	–	8.4
Ti_V	11.5	9.0	–	8.4
Ti_{IV}	–	–	6.4	–
μ_2-O	11.5	9.0	12.8	8.4
μ_3-O	11.5	9.0	–	8.4
N_{Ti-O}	23.0	18.0	25.5	16.8

N_{Ti-O} (in μmol m^{-2}) stands for the number of Ti–O bonds broken per surface area.

Table 3
Energetics of the dehydrated (hkl) surfaces before and after relaxation. Γ^0_{hkl} is defined by Eq. (4)

	hkl			
	001	100	110	101
Γ^0_{hkl} before relaxation (mJ m^{-2})	1034	1412	2031	1139
E_{Ti-O} before relaxation (kJ mol^{-1})	45	78	79	68
Γ^0_{hkl} after relaxation (mJ m^{-2})	984	533	1024	435
E_{Ti-O} after relaxation (kJ mol^{-1})	43	30	40	26

E_{Ti-O} is calculated by dividing Γ^0_{hkl} by N_{Ti-O} as defined in Table 2.

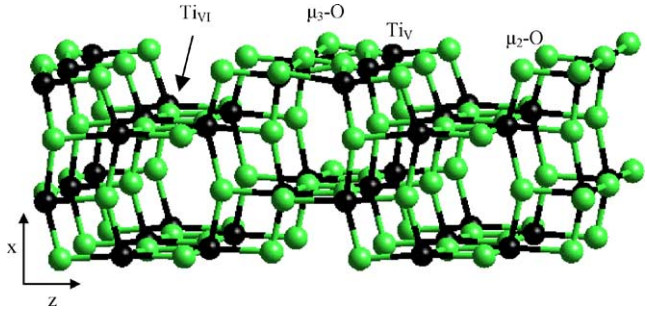

Fig. 3. Structure of the dehydrated (100) surface after relaxation ($\theta_{100}=0$). For the sake of clarity, only the four outmost layers are represented (same legend as Fig. 1).

surface. After relaxation, the surface energy is estimated at 984 mJ m^{-2}, revealing simultaneously a small relaxation energy of 50 mJ m^{-2}, as reported in Table 3. As a consequence, the structural relaxation remains moderate. The symmetry of the surface does not allow for oxygen atoms to move along the x and y directions. The oxygen relaxation along the z axis implies a slight expansion of the surface $(Ti–O)_{x,y}$ distance at about 1.96 Å.

3.2.2. (100) surface

The Lewis acid sites exposed after the cleavage are of Ti_V and Ti_{VI} types, while basic sites are of μ_2-O and μ_3-O types as represented in Fig. 3 and reported in Table 2. The number of broken Ti–O bonds (18.0 μmol m^{-2}) is lower than for the (001) surface. The relaxation energy of about 880 mJ m^{-2} is large for this surface. Furthermore, the relax-

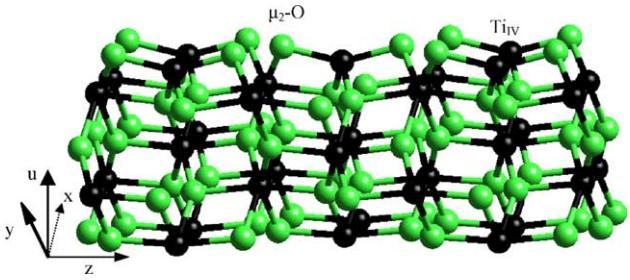

Fig. 4. Structure of the dehydrated (110) surface after relaxation ($\theta_{110} = 0$). For the sake of clarity, the five outmost layers only are represented (same legend as Fig. 1).

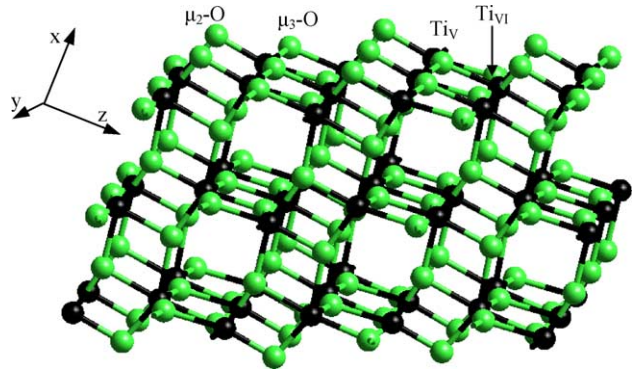

Fig. 5. Structure of the dehydrated (101) surface after relaxation ($\theta_{101} = 0$). For the sake of clarity, the five outmost layers only are represented (same legend as Fig. 1).

ation phenomenon depends on the parity of the number of layers. The surface energy oscillates with the number of layers and with a decreasing amplitude of the oscillations. For odd numbers of layers, the energy decreases toward the true value for a significantly larger slab thickness. This is due to the presence of a symmetry plane in the middle of the slab, preventing the atoms belonging to this plane from relaxing. A similar behavior was reported for the (110) surface of rutile [43]. As a consequence, quite a large number of layers is required to obtain a correct surface energy: we took the value obtained for 8 layers as a good estimate (533 ± 10 mJ m^{-2}). The Ti–O distances along the x and z axis become shorter (see Fig. 3): two $(\text{Ti–O})_x$, values are found at about 1.86 and 1.81 Å, while the $(\text{Ti–O})_z$ distance becomes equal to 1.84 Å.

3.2.3. (110) surface

Two types of sites are present on this surface after cleaving the bulk structure: Ti_{IV} sites and μ_2-O sites, corresponding to the highest number of Ti–O bonds broken (Fig. 4 and Table 2) per surface area. The variation of the surface energy as a function of the number of layers exhibits oscillations of the type observed for the (100) surface. We choose 8 layers for the surface energy calculation. Due to the low coordination of Ti and O atoms at the surface, the energy of the unrelaxed surface is the largest. Although the relaxation energy of about 1100 mJ m^{-2} is also the largest, the surface energy at about 1024 mJ m^{-2} remains the highest. The local structure of the surface is strongly modified upon relaxation: the surface Ti–O distances are found at 1.87 Å, while the first subsurface Ti–O distances are even shorter at 1.80 Å. Simultaneously, short Ti–Ti distances (2.88 Å) are formed within the surface plane.

3.2.4. (101) surface

As for the (100) surface, the (101) surface exhibits 4 types of Lewis sites: Ti_{V} and Ti_{VI} types as well as μ_2-O and μ_3-O sites (Table 2 and Fig. 5). At the same time, the number of Ti–O bonds broken per surface area is lower than for the (100) surface implying that the surface energy is also smaller. Furthermore, the effect of surface relaxation leads also to a significant decrease of the surface energy at 435 mJ m^{-2}. The outer surface $(\text{Ti–O})_x$ distances (resp. $(\text{Ti–O})_z$) decrease to 1.86 Å (resp. 1.84), while Ti–Ti distances in the surface plane also decrease to 2.86 Å upon relaxation.

3.2.5. Conclusion

Before geometry relaxation, we find results similar to those of Beltrán et al. [26] and obtain the following order for the surface energies: (001) < (101) < (100) ≪ (110). To explain this trend, we should analyze the nature of bonds broken at the surface. Generating the (100), (110), and (101) surfaces implies cleaving $(\text{Ti–O})_{x,y}$ bonds, whereas for the (001) surface, only $(\text{Ti–O})_z$ bonds are broken. In the bulk, the $(\text{Ti–O})_z$ bond length is longer than $(\text{Ti–O})_{x,y}$. If we define the Ti–O bond energy as the surface energy divided by the number of Ti–O bonds (see Table 3), we find that the surface $(\text{Ti–O})_z$ bond energy is intrinsically of about 45 kJ mol^{-1}, i.e., 30–35 kJ mol^{-1} weaker than $(\text{Ti–O})_{x,y}$ bonds, before relaxation. This is the reason why the (001) surface exhibits the lowest surface energy before relaxation.

However, as relaxation effects are crucial for a complete understanding of the energetic properties of surfaces, the aforementioned ranking is significantly modified after surface relaxation: (101) < (100) < (001) < (110). Beltrán et al. [26] observed that the (001) surface exhibits only modest relaxation while the (101) surface relaxed strongly. Our calculations confirm this trend and reveal that the (100) and (110) surfaces are also affected by strong relaxation effects. Even if the (110) surface is always the least stable surface, relaxation effects allow the (100) and (101) surfaces to gain such energies that their surface energy becomes lower than the (001) surface. The evaluation of the surface Ti–O bond energies (Table 3) put forward that the (001) and (110) surfaces exhibit similar high values (of about 40 kJ mol^{-1}) corresponding to the highest surface energies, while the (100) and (101) Ti–O bonds are about 10 kJ mol^{-1} weaker. As we will see further under Discussion, this is crucial for understanding the surface reactivities.

The equilibrium morphology, as given by the Gibbs–Curie–Wulff law (see Methods), depends on the surface energies for each orientation and on the symmetry rules of the solids. Figs. 6a and b show the morphology of the crystal-

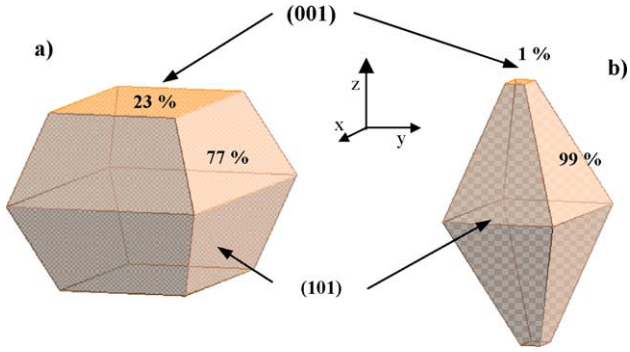

Fig. 6. Gibbs–Curie–Wulff morphologies of fully dehydrated anatase–TiO_2 nanocrystallite: (a) before relaxation and (b) after relaxation.

lite respectively before relaxation and after relaxation for the dehydrated surface. We find that even if the (100) surface exhibits a relatively low energy, this surface does not appear according to the Gibbs–Curie–Wulff rules. The morphology is a truncated bipyramid with a square basis, where the two exposed surfaces are the (101) and (001) surfaces. As is well known, the relaxation effects are crucial for determining the correct shape. Upon relaxation, the proportion of the (001) surface decreases from 23 to 1%. This shape of the anatase crystallites agrees well with those observed by Chemseddine and Moritz [10] or Ohno et al. [12] using electron microscopy techniques. At this stage, it must be stressed that the aforecalculated equilibrium morphologies do not take into account corner and edge contributions. Actually, to investigate this effect remains beyond the scope of the present work, because it is directly linked to size effects. According to our approach, we assume that corner and edge energies are not high enough to modify the equilibrium morphology, which seems to be reasonable for particle sizes observed experimentally.

However, according to experimental and theoretical studies of various systems, it is known that the experimental conditions may influence strongly the equilibrium morphologies [3,27–29]. For that reason, in the next section, we investigate the effect of partial pressure of water and temperature.

3.3. Effect of hydration on surface structures and energies

The thermodynamic approach proposed in the methodology part for investigating hydration effects requires that for each coverage, θ_{hkl}, the stable adsorption modes of water are determined. Among these modes, water may be first chemisorbed in a nondissociated state on one titanium Lewis acid site. Water may then dissociate on one titanium site and one Lewis basic oxygen site leading to the formation of two new hydroxyl groups at the surface. The third adsorption mode (occurring at high water coverage) is the physisorption of water molecules at the previously formed OH surface groups involving hydrogen bonding. For each coverage, the most stable configuration is determined by the calculation of adsorption energies, as defined in Eq. (5).

In the following, we call μ_1-OH all hydroxyl groups where the oxygen atom is monocoordinated with one surface aluminum atom, μ_2-OH a twofold coordinated hydroxyl group, and μ_1-OH_2 a nondissociated chemisorbed water molecule.

3.3.1. (001) surface

The main results concerning the (001) surface are presented in Fig. 7 which shows the variation of the adsorption energy of water as a function of θ. The calculations show that water is mainly dissociated. The adsorption energy varies strongly with increasing coverage from -165 to -101 kJ mol^{-1}. At a low coverage, because of the formation of two iono-covalent bonds, i.e., Ti_V–OH and O–H, the adsorption energy is the highest. The mechanism leading to the

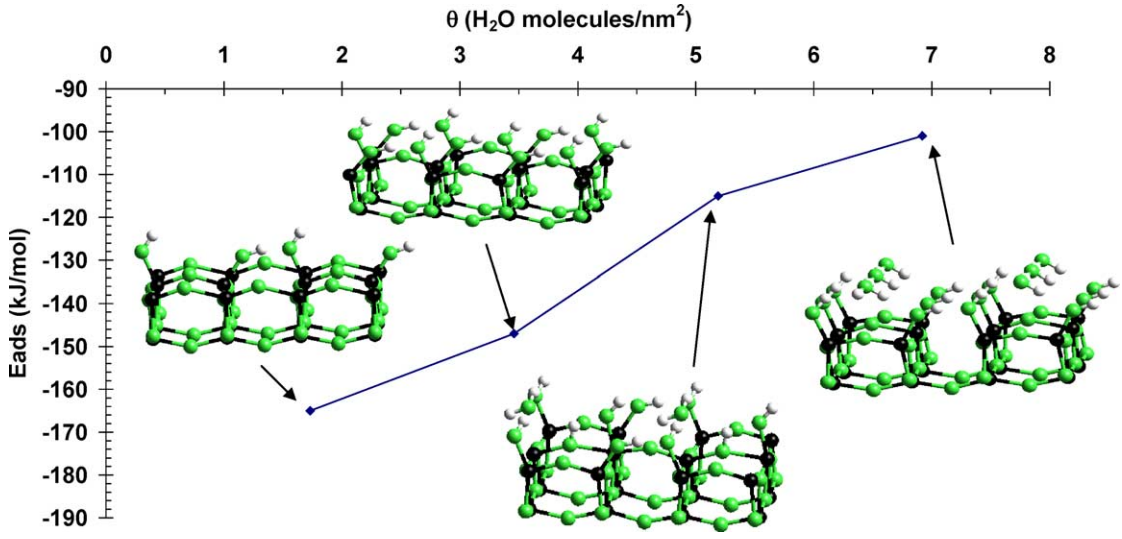

Fig. 7. Adsorption energy of water on the (001) surface as a function of coverage (black balls, titanium atoms; gray balls, oxygen atoms; white balls, hydrogen atoms). n.b.: Insets give a ball and stick representation of the local structures.

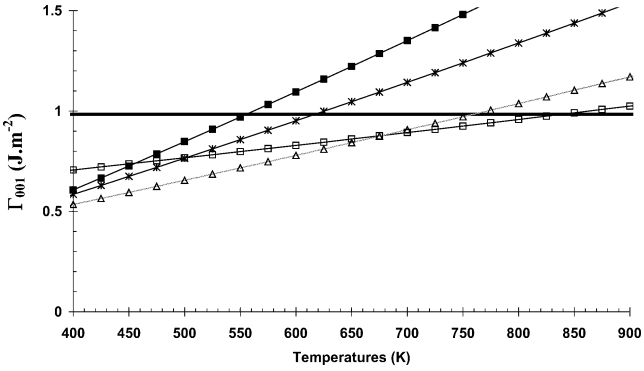

Fig. 8. (001) surface energy as a function of the temperature (at standard vapor pressure, p_0), calculated according to Eq. (3). Each straight line corresponds to the following water coverages: (—) $\theta_{001} = 0.0$ $H_2O\,nm^{-2}$; (□) $\theta_{001} = 1.7$; (Δ) $\theta_{001} = 3.5$; (∗) $\theta_{001} = 5.2$; (■) $\theta_{001} = 6.9$.

dissociation of the water molecule is complex and induces a reorganization of the surface atoms. For $\theta = 1.7$ OH nm^{-2} and $\theta = 3.5$ OH nm^{-2}, the dissociation of H_2O leads to the surface Ti–O bond breaking, and the simultaneous formation of one strong intramolecular hydrogen bond between the two newly formed hydroxyl groups (see inset of Fig. 7). These results are in qualitative agreement with the Hartree–Fock calculations of Fahmi and Minot [25] and quantitatively with the DFT-GGA calculations of Vittadini et al. [44], also showing that the dissociated state is stable versus the undissociated one. At a coverage greater than 3.5 OH nm^{-2}, mixed structures combining dissociated and nondissociated adsorbed H_2O, as represented in the second inset of Fig. 7, can be stabilized. However, the adsorption energy becomes smaller corresponding to physisorbed states. This is again consistent with the results of Vittadini et al. [44] who also found a stable mixed state. It can be underlined that when increasing the hydration of the surface, the chemisorbed nondissociated states of water become closer in energy to the dissociated state due to a decrease of the number of available Lewis sites and to an increase of hydrogen bonds.

Fig. 8 represents the variation of the surface energy as a function of temperature for a standard water pressure (i.e., $p_0 = 1.013$ bar), as expressed by Eq. (3). Each straight line corresponds to one water coverage detailed previously and for which the adsorption energy is given in Fig. 7. The horizontal thick line represents the fully dehydrated surface, as described in the previous section, and corresponds to a surface energy of 984 mJ m^{-2}. On such a diagram, the most stable state is given by the lowest surface energy value at a given temperature. For standard p_{H_2O} and temperatures between 400 and 680 K, the stable surface water coverage is 3.5 OH nm^{-2} represented by the line with triangular symbols. When the temperature rises at 840 K, the coverage decreases to 1.7 OH nm^{-2} (line with squared symbols) due to water desorption. Above 840 K, all water molecules are removed from the surface leading to the dehydrated state studied in the previous section.

Table 4
Type of surface species for T in the range of 600–700 K and $p_{H_2O}/p_0 = 1$ (○), $p_{H_2O}/p_0 = 0.01$ (×) as a function of the crystallographic orientation

	hkl			
	001	100	110	101
Ti_{VI}	–	○ ×	–	○ ×
Ti_V	○ ×	○ ×	×	○ ×
Ti_{IV}	–	–	×	–
μ_1-OH_2	–	–	–	–
μ_1-OH	○ ×	–	○ ×	–
μ_2-OH	–	–	○ ×	–
μ_2-O	○ ×	○ ×	○ ×	○ ×
μ_3-O	○ ×	○ ×	–	○ ×

Table 5
Calculated stretching frequencies of various OH groups as a function of the surface orientation

OH type	Orientation	θ_{hkl} ($H_2O\,nm^{-2}$)	d_{OH} (Å)	ω_{calc} (cm^{-1})	ω_{exp} (cm^{-1})
Ti_V–μ_1OH	(001)	$\theta_{001} = 1.7$	0.988	3760	3730–3742
Ti_V–μ_1OH		$\theta_{001} = 3.5$	0.989	3746–3751	
Ti_V–μ_1OH	(110)	$\theta_{110} = 3.8$	0.990	3728	3725
Ti_{VI}–μ_1OH_2	(100)	$\theta_{100} = 8.2$	0.992	3710	3715
Ti_{VI}–μ_1OH		$\theta_{100} = 8.2$	0.992	3688	3690
Ti_{VI}–μ_1OH_2	(101)	$\theta_{101} = 10.1$	0.993	3665	3620–3680
Ti_{VI}–μ_1OH_2		$\theta_{101} = 10.1$	0.994	3646	
Phys. H_2O		$\theta_{101} = 10.1$		2950–3253	3300
Ti_V–μ_1OH_2/ phys. H_2O	(101)	$\theta_{101} = 10.1$	0.990	1565–1646	1600–1640
Ti_{VI}–μ_1OH_2/ phys. H_2O	(100)	$\theta_{100} = 8.2$	0.990	1578–1648	

The experimental values are collected from various published experimental works [15–20].

The analysis of the surface species is given in Table 4, for an interval of temperature between 600 and 700 K, and corresponding to hydrotreating conditions. We see that for the (001) surface, Brønsted sites are of Ti_V–μ_1-OH types. Acid Lewis sites are of Ti_V types and basic Lewis sites of μ_2-O as well as μ_3-O types. As a corollary, the high water coverage (6.9 OH nm^{-2} with physisorbed water) can only be reached for lower temperatures or significantly higher pressure. As a consequence, if the (001) surface exists (see further) under hydrotreating conditions, it contains a rather high amount of hydroxyl groups representative of Brønsted acid sites.

The vibrational analysis of the stretching frequencies of the two types of OH groups is reported in Table 5. The highest calculated frequency is at 3760 cm^{-1} and corresponds to free Ti_V–μ_1-OH at low water coverage. When the coverage increases (3.46 $H_2O\,nm^{-2}$), the frequency of those OH groups is shifted downward at 3746–3751 cm^{-1}. This mode may be assigned to the experimental value found between 3730 and 3745 cm^{-1} according to several experimental studies [15–18,20]. It must be underlined that a low-frequency mode (calculated at around 2300 cm^{-1}) corresponds to the second Ti_V–μ_1-OH group, exhibiting a strong hydrogen

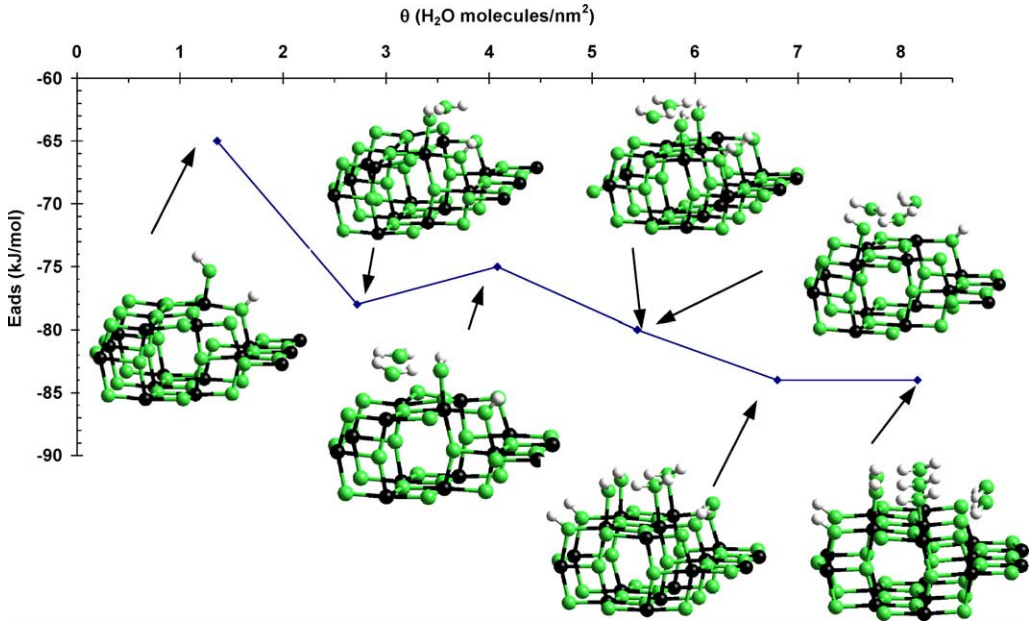

Fig. 9. Adsorption energy of water on the (100) surface as a function of coverage (same legends as in Fig. 7).

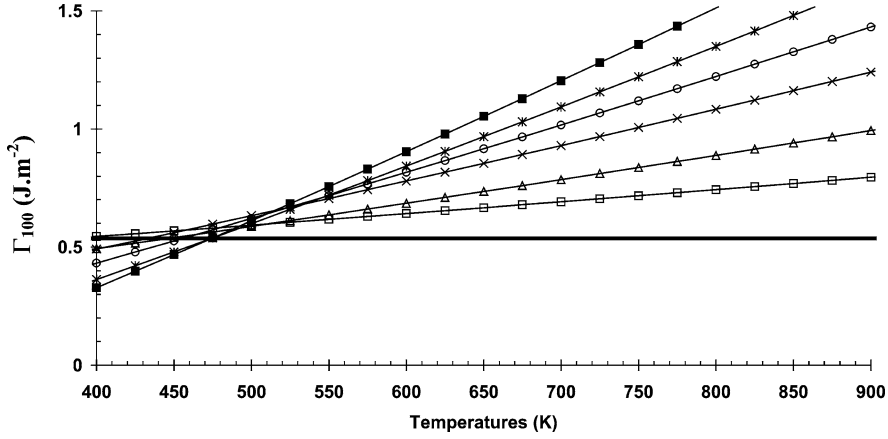

Fig. 10. (100) surface energy as a function of the temperature (at standard vapor pressure, p_0), calculated according to Eq. (3). Each straight line corresponds to the following water coverages: (—) $\theta_{100} = 0.0$ $H_2O\,nm^{-2}$; (□) $\theta_{100} = 1.4$; (Δ) $\theta_{100} = 2.7$; (×) $\theta_{100} = 4.1$; (○) $\theta_{100} = 5.4$; (∗) $\theta_{100} = 6.8$; (■) $\theta_{100} = 8.2$.

bond with the oxygen belonging to the previous neighboring hydroxyl group. To our knowledge, this band at 2300 cm^{-1} has never been reported in IR spectra. At this stage of our work, we cannot furnish a definite explanation on this result which might be attributed either to a lack of detailed experimental data in this spectra region or to a limitation of our DFT calculations in the case of strong hydrogen bonding.

3.3.2. (100) surface

The results of the hydration process of the (100) surface are represented in Figs. 9 and 10 in a similar way as for the previous case. Adsorption energies are between −65 and −84 kJ mol^{-1}, and are significantly lower than for the (001). This is directly connected to the fact that the surface Ti–O bond energy after relaxation, as reported in Table 3, is weaker. The surface reactivity, regarding water adsorption, is thus weaker. Besides, it should be underlined that many metastable states (combining dissociated and nondissociated configurations) found at different water coverages are all very close in energy (less than 10 kJ mol^{-1}). For instance, at $\theta = 1.4$ $H_2O\,nm^{-2}$, the nondissociated configuration is only 5 kJ mol^{-1} less stable than the dissociated configuration reported in the inset of Fig. 9. As a consequence, it can be difficult to determine the true stable configurations of water on this surface. At higher coverages, mixed structures of dissociated and undissociated states are found to be more stable than fully dissociated structures (see the two insets of Fig. 9 for $\theta = 5.44$). However, the energy difference between those configurations is narrow.

Focusing on the stable states as a function of temperature (Fig. 10), the (100) surface exhibits a contrasted behavior in comparison with the (001). As soon as the temperature exceeds 450 K, this surface is dehydrated at standard water pressure. For T smaller than 450 K, the surface exhibits

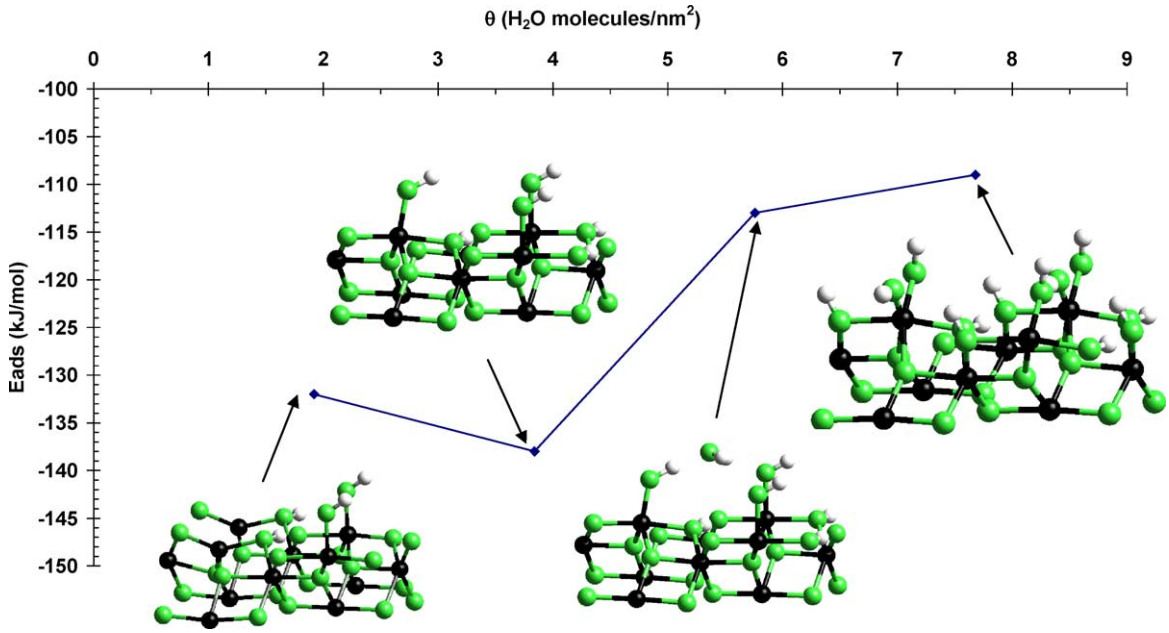

Fig. 11. Adsorption energy of water on the (110) surface as a function of coverage (same legend as in Fig. 7).

water coverages of 8.2 $H_2O\,nm^{-2}$. According to the low adsorption energy, the adsorbed molecules are easily removed from the surface. When the pressure decreases, the dehydration temperature drops simultaneously. As a consequence, assuming that this surface is present under working conditions, Lewis acid sites of Ti_V and Ti_{VI} types with Lewis basic sites of μ_2-O and μ_3-O are stabilized (Table 4). However, no hydroxyl groups (i.e., Brønsted sites) can be thermodynamically stabilized under low water pressure and for temperatures between 600 and 700 K (in particular under hydrotreating conditions).

For this surface containing 8.2 $H_2O\,nm^{-2}$, the vibrational analysis (Table 5) indicates that the two highest frequency values at about 3688 cm^{-1} (resp. 3710 cm^{-1}) correspond to Ti_{VI}–μ_1-OH groups (resp. to one of the OH group belonging to a water molecule chemisorbed on Ti_{VI} atoms). We find that $\omega(Ti_{VI}\text{–}\mu_1\text{-OH})_{100} < \omega(Ti_V\text{–}\mu_1\text{-OH})_{001}$, confirming the stronger Brønsted basicity of Ti_V–μ_1-OH species. It should also be noted, that the mode at 3710 cm^{-1} corresponds to a chemisorbed water molecule, traditionally expected at lower frequency. This is due to the specific interaction of the water molecule with a neighboring OH group (see insets in Fig. 9).

3.3.3. (110) surface

The results of the hydration process of the (110) surface are represented in Figs. 11 and 12. As shown in the previous section, the dehydrated (110) surface exhibits Ti_{IV} which are possible sites for water dissociation. Furthermore, the surface Ti–O bond energy is rather close to the value of the (001) surface (Table 3), implying that the surface reactivity toward water is expected to be high. Fig. 11 confirms indeed that the adsorption energies of water are similar to those on the (001) surface: between −138 and −109 kJ mol^{-1}. For

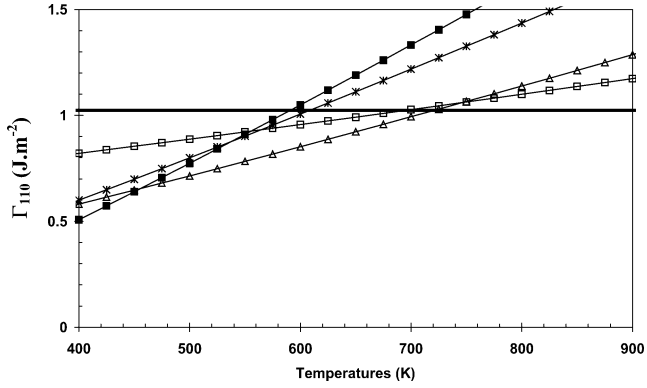

Fig. 12. (110) surface energy as a function of the temperature (at standard vapor pressure, p_0), calculated according to Eq. (3). Each straight line corresponds to the following water coverages: (—) $\theta_{110} = 0.0$ $H_2O\,nm^{-2}$; (□) $\theta_{110} = 1.9$; (Δ) $\theta_{110} = 3.8$; (∗) $\theta_{110} = 5.8$; (■) $\theta_{110} = 7.7$.

hydroxyl coverages lower than 3.8 $H_2O\,nm^{-2}$, water dissociates on one Lewis acidic and one basic site resulting in the formation of Ti_V–μ_1-OH and μ_2-OH groups (see first inset of Fig. 11). The complete hydration of the surface is obtained for $\theta = 7.7$ $H_2O\,nm^{-2}$. The intermediate coverage at 5.8 $H_2O\,nm^{-2}$ does not allow a complete dissociated state, preferring mixed configurations with physisorbed water. As for the (001) surface, when increasing water content, physisorbed states may compete with dissociated states due to the increase of the stabilizing hydrogen bonds.

As expected and according to the value of adsorption energies, this surface remains hydrated for temperatures up to 710 K at standard pressure (Fig. 12). Two transition temperatures are found on the surface energy diagram. Up to 460 K, the surface is fully saturated (7.7 $H_2O\,nm^{-2}$). The two types of hydroxyl groups are Ti_{VI}–μ_1-OH and (Ti_{VI},Ti_{VI})–μ_2-OH.

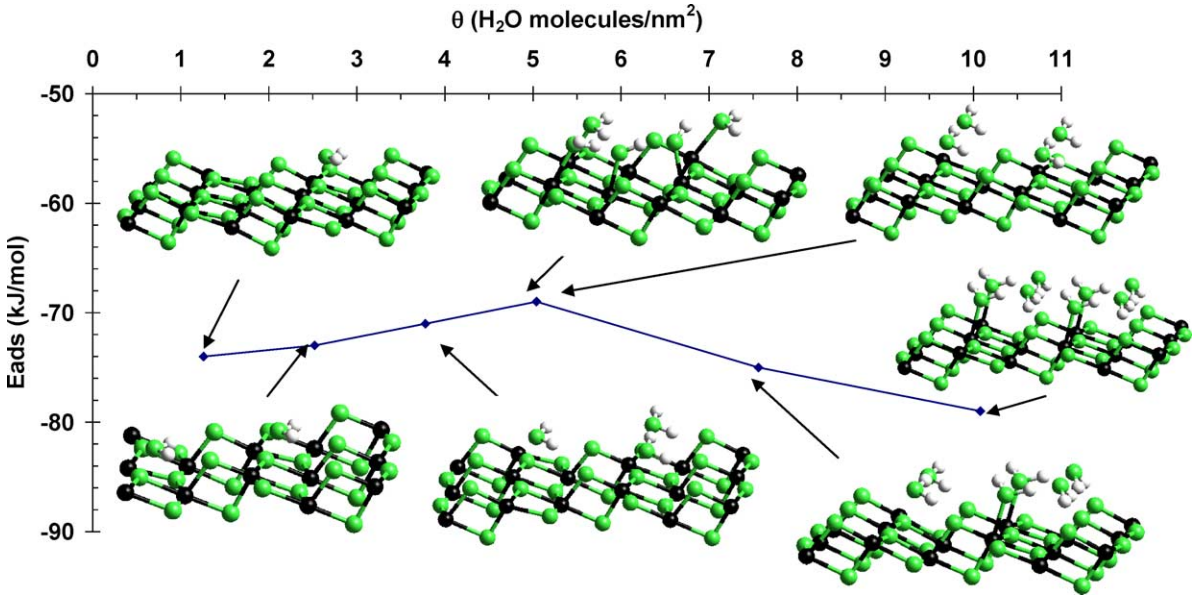

Fig. 13. Adsorption energy of water on the (101) surface as a function of coverage (same legend as in Fig. 7).

At 460 K, the first transition occurs leading to a coverage of 3.8 $H_2O\,nm^{-2}$ which remains stable up to 710 K. The types of hydroxyl groups are Ti_V–μ_1-OH and (Ti_V,Ti_{VI})–μ_2-OH. The dehydration temperature of the surface corresponds to 710 K, rather close to that of the (001) surface: hence, the reactivities of the two surfaces are similar. For working conditions corresponding to hydrotreating conditions, Brønsted sites of Ti_V–μ_1-OH and (Ti_V,Ti_{VI})–μ_2-OH types as well as Lewis sites are present (Table 4).

The stretching frequency of Ti_V–μ_1-OH groups stable between 460 and 700 K is estimated at 3728 cm^{-1}, which may be assigned to the peak at about 3725 cm^{-1} reported in [16], assuming the existence of the (110) surface.

3.3.4. (101) surface

According to Fig. 13, water molecules are chemisorbed without dissociation. The adsorption energies between −79 and −69 kJ mol^{-1} remain close to the value obtained for the (100) surface. This is again not surprising when considering the surface Ti–O bond energy (Table 3), very close to that of (100) surface. As a consequence, the reactivity of this surface toward water adsorption is rather low as for the (100) orientation. For water coverages equal to 5.0 $H_2O\,nm^{-2}$, the Lewis Ti_V sites are saturated by one chemisorbed water molecule (inset of Fig. 12). For higher coverages, new water molecules can only be adsorbed through hydrogen bonds: the hydrogen atoms of water interacting with the basic Lewis μ_2-O sites. The saturation coverage is thus reached for $\theta = 10.1$ $H_2O\,nm^{-2}$. It is interesting to note that hydrogen-bonded molecules strengthen the interaction of the chemisorbed ones, leading to an increase of the adsorption energy. To some extent, this result can be compared to that of Giordano et al. reported on the (100) MgO surface, showing that the formation of hydrogen bonds may enhance the water adsorption and dissociation [45]. At $\theta = 5.0$ $H_2O\,nm^{-2}$, we find that the fully nondissociated state and the fully dissociated configurations can compete in energy within less than 7 kJ mol^{-1}. Regarding the local structure of the surface and adsorption energies, the results obtained for this surface are in quite good agreement with those of Vittadini et al. [44], except that the latter did not report the possible competition between dissociated and nondissociated states at $\theta = 5.0$ $H_2O\,nm^{-2}$.

Analyzing the effect of temperature on surface hydration (Fig. 14) reveals that the (101) surface is completely dehydrated above 450 K for standard water pressure, as for the (100) surface. At ambient temperature, the stable coverage is 10.8 $H_2O\,nm^{-2}$, and no Lewis site is available. The surface exhibits Ti_{VI}–μ_1-OH_2 species together with physisorbed water molecules. The dehydration temperature for the dehydrated surface drops to 375 K for $p_{H_2O}/p_0 = 0.01$. As a consequence, under hydrotreating conditions, the surface exhibits mainly Lewis sites (Table 4).

The analysis of the OH-stretching modes (Table 5) indicates that at $\theta = 10.8$ $H_2O\,nm^{-2}$, two frequencies are present at 3646 and 3665 cm^{-1}. They correspond to free OH groups belonging to water molecules chemisorbed on Ti_{VI} atoms. We propose that the IR bands observed in the range 3620–3680 cm^{-1} [15,17,18,20] be assigned to these groups. We find the bending modes of chemisorbed and physisorbed water molecules around 1565–1646 cm^{-1}, explaining experimental observations from [15–17]. These modes were also obtained for water molecules on the (100) surface. Finally, we find several OH-stretching frequencies around 2950–3253 cm^{-1}, corresponding to water molecules adsorbed through hydrogen bonds on this surface, as observed experimentally at about 3300 cm^{-1}.

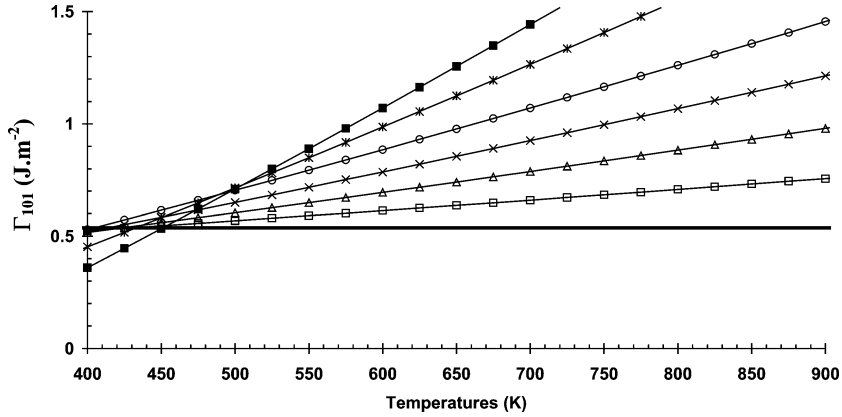

Fig. 14. (101) surface energy as a function of the temperature (at standard vapor pressure, p_0), calculated according to Eq. (3). Each straight line corresponds to the following water coverages: (—) $\theta_{101} = 0.0$ $H_2O\,nm^{-2}$; (□) $\theta_{101} = 1.3$; (Δ) $\theta_{101} = 2.5$; (×) $\theta_{101} = 3.8$; (○) $\theta_{101} = 5.1$; (∗) $\theta_{101} = 7.6$; (■) $\theta_{101} = 10.1$.

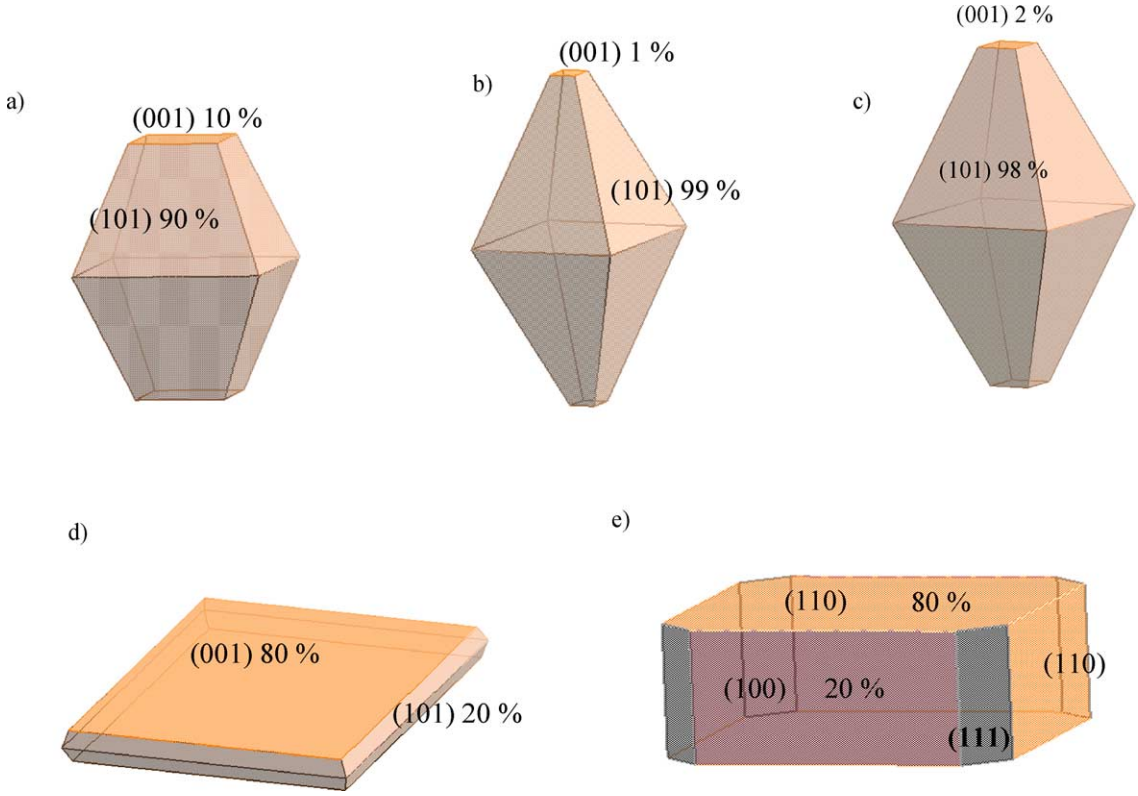

Fig. 15. Morphologies of anatase and γ-alumina under different working conditions and thermodynamic states. TiO_2–anatase at equilibrium for $p_{H_2O}/p_0 = 0.01$, (a) $T = 400$ K and (b) $T = 700$ K; for $p_{H_2O} = p_0$, (c) $T = 400$ K or $T = 700$ K. (d) Hypothetical metastable state of anatase–TiO_2. (e) γ-Alumina morphologies inherited from boehmite (in the present work, we neglect the (III) surface).

3.4. Effect of hydration on equilibrium morphologies

We have determined so far the surface energy of the four low index crystallographic orientations of anatase as a function of temperature and partial pressure of water. Applying the values of Figs. 8, 10, 12 and 14 in the Gibbs–Curie–Wulff law (Eq. (1)), we deduce the equilibrium morphologies as a function of the working conditions. For three typical conditions, the shapes are drawn in Figs. 15a, 15b, and 15c, revealing first that at thermodynamic equilibrium, the morphology exhibits only the (101) and (001) facets, whatever the pressure and temperature. The temperature and pressure variations do not allow the appearance of the (110) or (100) facets. However, slight changes in the proportions of the (101) and (001) surface areas are induced by temperature or pressure effects. For low water pressure ($p_{H_2O}/p_0 = 0.01$), increasing the temperature favors the (101) surface (see Figs. 15a and 15b). This is due to the removal of OH groups located on the (001) plane, implying an increase of its surface energy (Fig. 8), and consequently a decrease in area of this plane. Conversely, at a given temperature, an increase of p_{H_2O} may favor either the (101) or the (001) orientation

due to the competitive stabilizing effect of water adsorptions on the two planes.

4. Discussion

At this stage, it is worth underlining that the calculated equilibrium morphology together with the OH-stretching analysis is compatible with the observed IR bands. Although it is difficult to know precisely the experimental conditions or pretreatment (T and water pressure) undergone by anatase samples before and during IR analysis, in what follows we attempt to confront experimental data with our simulations by taking into account temperature and vapor pressure effects, when available in the literature. The two main OH bands observed experimentally and reported in the literature are at 3730–3745 and 3620–3680 cm^{-1}, respectively [15–18,20]. According to the results of the previous section, we propose that the highest frequency corresponds to Ti_V–μ_1-OH groups located on the (001) surface, whereas the lowest one is assigned to the OH-stretching mode of water molecules chemisorbed on the (101) surface. Thus, we can expect that the modifications of the anatase–TiO_2 nanocrystallite morphologies at the preparation step may be monitored according to the relative intensities observed in IR. Moreover, other peaks (such as those calculated at about 3688, 3710, and 3725 cm^{-1}) might appear due to the existence of the (110) and (100) surfaces, such as observed in [15–17], if specific experimental conditions allow their stabilization.

Our results are also compatible with experimental observations by Morterra [17] related to the bending mode at about 1620 cm^{-1}. According to our calculations, chemisorbed water molecules can no longer exist above 450 K either on the (101) or on the (100) surfaces, explaining why this mode vanishes almost completely above 458 K in [17]. Furthermore, Munuera et al. observed that the formation of this mode upon increasing water coverage is correlated with stretching modes around 3620 and 3680 cm^{-1} [15], which is also in agreement with the calculated stretching frequencies found on the (101) surface at high coverages. TPD spectra by Munuera et al. also reveal that the first desorption peak at about 400 K may correspond to chemisorbed water molecules located on the (101) surface. According to [15], no correlation was found between the bending mode and the highest OH-stretching peak: we explain that phenomenon by the fact that this mode is the signature of the OH species formed on the (001) surface after water dissociation. Our calculations indicate that these OH groups should be completely removed from the (001) surface above 840 K. This may correspond to the high temperature peaks shown by TGA and TPD spectra at 723 K [15]. Intermediate TPD peaks (493–573 K) may correspond to the partial removal of hydroxyls from the (001) surface leading to intermediate coverages.

To further enrich the discussion on our results, the values of surface energies, Γ_{hkl}, are plotted as a function of T and p_{H_2O} in two-dimensional diagrams, such as in Fig. 16. These diagrams use a black–gray–white tone scale to visualize the Γ_{hkl} values. On the different toned regions, the hydroxyl coverages, θ, are also indicated. We use a similar representation for the (100) and (110) facets of the γ-alumina nanoparticles. The values used in Figs. 16e and 16f correspond to surface states determined by M. Digne et al. in [30] with energetic values expressed within the DFT-GGA-PAW approximation (see Methods) so that we can compare the hydroxylation of the two systems in a consistent way. As already noted by Digne et al. [30], the two γ-alumina surfaces exhibit distinct behaviors with respect to hydroxylation. While the (100) surface is completely dehydrated under hydrotreating conditions, the (110) surface retains a hydroxyl coverage of about 3–4.4 OH nm^{-2} (Figs. 16e and 16f). The surface energy of the (110) plane is significantly higher than that of the (100) plane, due to the lower coordination number of aluminum atoms present on this surface. As explained in detail in [30], the (110) contains Al_{IV} atoms to which OH groups are strongly bonded. For anatase–TiO_2, our calculations put forward two distincts families of facets. On the one hand, the (101) and the (100) surfaces are poorly reactive toward water and are dehydrated under hydrotreating conditions (Figs. 16a and 16d). Hence, regarding hydroxyl contents, these two surfaces of anatase behave similarly to the (100) surface of γ-alumina. This implies that this group of three surfaces, with low dehydration temperature, mainly exhibits Lewis acid–basic properties under hydrotreating conditions. On the contrary, the (110) surface of γ-alumina retains a significant amount of Brønsted acid sites under the same working conditions.

The (001) and (110) surfaces of anatase exhibit an intermediate behavior. They are only partially dehydrated under hydrotreating conditions with hydroxyl coverages between 0 and 1.7 OH nm^{-2} and 0 and 3.8 OH nm^{-2}, respectively (Figs. 16b and 16c). This is due to the presence of Ti_V atoms exhibiting stronger bond energies with OH groups. As underlined in the previous part, the two families of surfaces can be understood by a comparison of the surface Ti–O bond energy after relaxation, representing the intrinsic surface reactivities towards water. In Table 3, we note that the ordering of the Ti–O bond energy after relaxation, $E_{Ti–O}$, is the following:

$$(101) < (100) \ll (110) < (001).$$

As shown in Fig. 17, the dehydration temperatures under atmospheric water pressure follow the same ordering, meaning that the stronger the surface Ti–O bond energy, the more difficult the water removal. It is also interesting to underline that the two γ-alumina surfaces with Al–O energy calculated in the same way can also be included in the correlation. This is all the more surprising as other types of interaction such as hydrogen bonding (not directly accounted for in the M–O bond energy) may influence the dehydration process. This

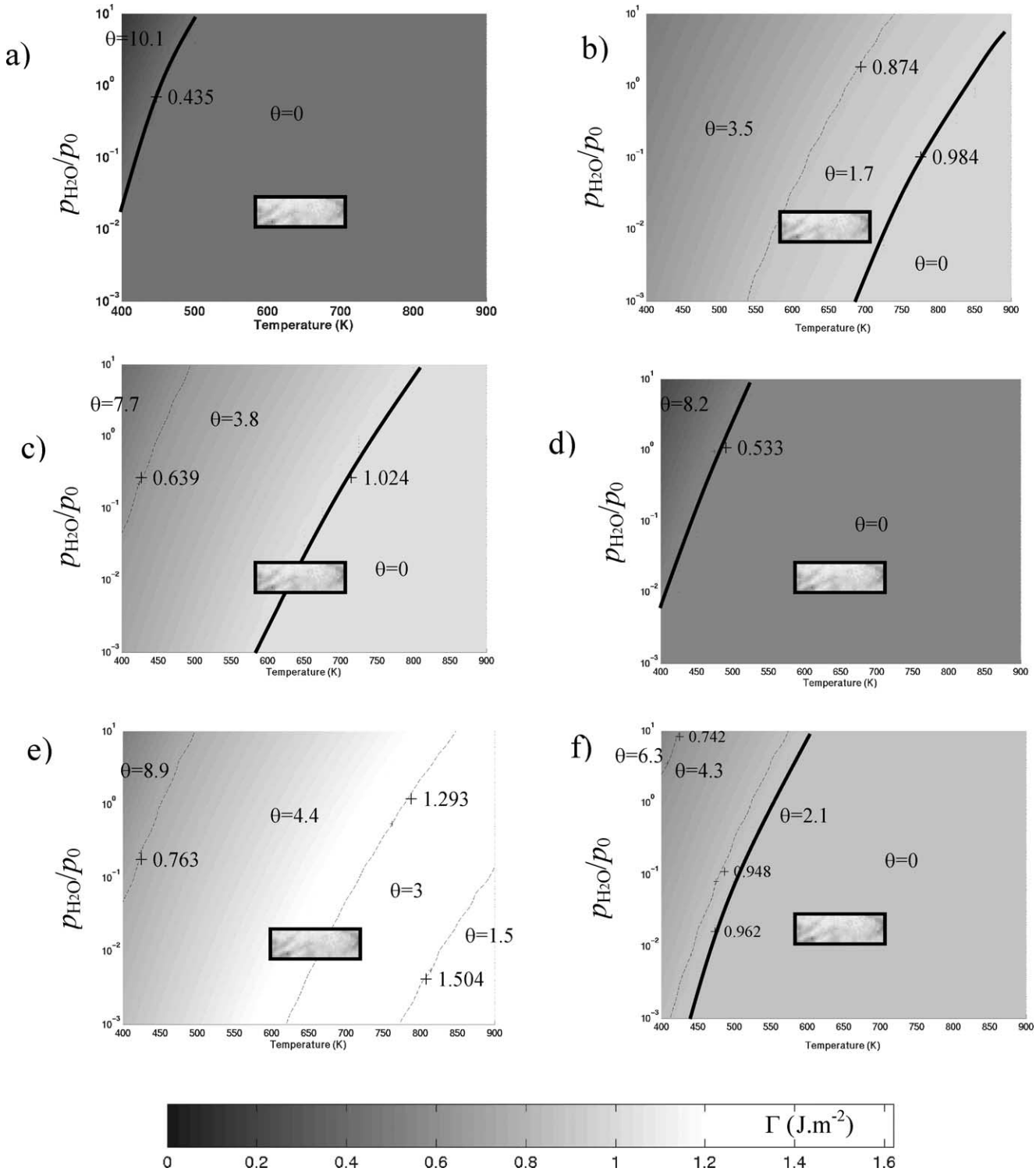

Fig. 16. (Γ, P, T) diagrams representing the isovalues of surface energy as a function of T and P_{H_2O} for different surfaces: (a) TiO_2 (101) surface, (b) TiO_2 (001) surface, (c) TiO_2 (110) surface, (d) TiO_2 (100) surface, (e) γ-Al_2O_3 (110) surface, (f) γ-Al_2O_3 (100) surface. Values for θ_{hkl} are also reported on the different domains.

means that the metal–oxygen bond strength represents the first-order contribution to the dehydration temperature.

A final concern is about the global content of hydroxyl groups of anatase–TiO_2 compared to γ-alumina. Here, the effect of morphology of the nanoparticles must be considered carefully. Table 6 reports the global surface hydroxyl concentration of the nanoparticles for various morphologies drawn in Fig. 15. For anatase–TiO_2, if considering first the equilibrium morphology, the increase of temperature or decrease of water pressure drastically diminishes the hydroxyl

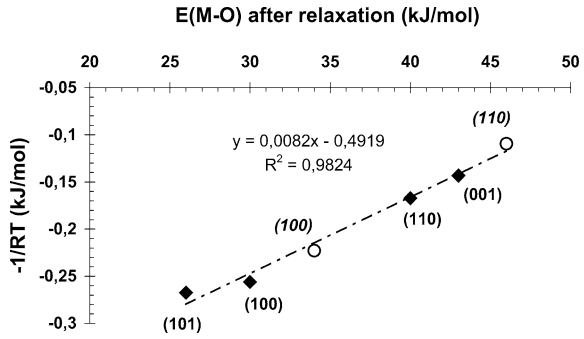

Fig. 17. Correlation between the inverse of dehydration temperature (at atmospheric pressure) and the surface metal–oxygen bond energy (after relaxation). (○) γ-Alumina, (◆) anatase–TiO_2.

Table 6
Surface hydroxyl concentration, θ_{tot}^{OH} (OH nm^{-2}), for different morphologies of anatase TiO_2 and comparison with γ-Al_2O_3 for two vapor pressures

Type of support—morphology	p_{H_2O}/p_0	$T = 400$ K	$T = 600$ K	$T = 700$ K
TiO_2—equilibrium	1	19.9 (Fig. 15a)	0.3	0.16 (Fig. 15b)
	0.01	0.7 (Fig. 15c)	0.1	0.05 (Fig. 15c)
TiO_2—metastable (001) 80% and (101) 20%, Fig. 15d	1	9.6	5.5	2.8
	0.01	5.5	2.8	2.8
TiO_2—metastable (001) 50% (110) 50%	1	11.1	7.3	5.6
	0.01	11.1	5.6	1.7
γ-Al_2O_3—metastable (inherited from boehmite) (110) 80% (100) 20%, Fig. 15e	1	15.9	7.1	7.1
	0.01	8.8	7.1	4.7

content. In particular, close to hydrotreating conditions, the hydroxyl concentration is low, at about 0.1 OH nm^{-2} and results exclusively from the contribution of the (001) facet. This value is significantly lower than the concentration on γ-alumina (about 5 OH nm^{-2}) under the same conditions.

This result is explained, on the one hand, by the fact that OH groups attached to Al_{IV} or Al_V sites are more stable than Ti_V–OH, Ti_{VI}–OH, or Ti_{VI}–OH_2. On the other hand, it is also due to a morphology effect. Indeed, γ-alumina nanoparticles used as catalytic support are obtained by a dehydration–calcination process of the boehmite (AlOOH) precursor. As a consequence, the γ-alumina shapes are inherited from boehmite particles following topotactic rules for the transformation [30,46]. Experimentally [47], it is known that the (110) facet represents about 80% of the external surface, while the (100) facet represents about 20% (Fig. 15e). With this facet distribution, the γ-alumina particles has a metastable morphology inherited from the boehmite precursor. This implies that the OH contents of γ-alumina particles are significantly increased by the predominant presence of the high-energy (110) surface. In the case where the particles would be at an equilibrium shape, the surface carrying basic OH species would not be the major one, and its hydroxyl content would thus be significantly lower. If experimental conditions can be found for stabilizing anatase morphologies with 80% of (001) and 20% of (101) such as represented in Fig. 15d, the global OH contents can be significantly increased to about 2.8 OH nm^{-2}. Other scenarii can be imagined to favor the (110) surface (Table 6). Such metastable morphologies must be sought, if one aims at enhancing exchangeable basic OH species.

5. Conclusion

This work based on density functional calculations investigated the surface properties of anatase–TiO_2, a material investigated as a prospective and promising support for hydrotreating catalysts. By coupling ab initio calculations and a thermodynamic model, we have determined the hydration state (type of hydroxyl groups) under various working conditions controlled by the temperature and pressure of water. The characterization of Brønsted acid sites is furnished by means of local structure optimizations and vibrational analysis of the OH-stretching bonds. This enables the assignment of different types of OH bands observed by IR. In particular, the highest frequency band is attributed to Ti_V–μ_1-OH groups located on the (001) surface and the band at about 3620–3680 cm^{-1} to Ti_{VI}–OH_2 located on the (101) surface. This assignment is consistent with the bending mode of chemisorbed water on the (101) surface. The morphology analysis is also compatible with such an assignment, electron microscopy observations, and TPD experiments reported in the literature. A consistent comparison with recent results obtained on γ-alumina allows general concepts on the hydration processes of these two relevant oxidic supports to be derived. Regarding the hydroxylation state of nanoparticles of the two supports under hydrotreating conditions, we put forward three distinct types of surface. The surfaces dehydrated at low temperature are the (101) and (100) surfaces of anatase and the (100) of γ-alumina. The (110) surface of γ-alumina is dehydrated at high temperatures. An intermediate behavior is revealed by the (001) and (101) surfaces of anatase remaining partially hydrated at high temperatures. As a consequence for the synthesis of the anatase–TiO_2 support, one should favor morphologies exposing the high energy (001) and (110) surfaces, if one seeks to enhance the basic hydroxyl content of the support. Indeed, knowledge of these exchangeable hydroxyls will be crucial for a better control of the interaction between the support and the active phase precursors, which may have a direct influence on the final hydrodesulfurization activity.

Acknowledgments

The authors are grateful to S. Dzwigaj from the Université Paris VI (France) and C. Geantet from the Institut de Recherche sur la Catalyse de Lyon (France) for fruitful discussions. They also thank their IFP colleague J. Lynch for carefully reading the paper. C. Arrouvel would also like to

thank R. Scheichl from the University of Bath (UK) for his kind help in using the Matlab software. This work has been undertaken within the Groupement de Recherche Européen Dynamique Moléculaire Quantique Appliquée à la Catalyse, a joint project of IFP-CNRS-TOTAL-Universität Wien.

References

[1] H. Topsøe, B.S. Clausen, F.E. Massoth, in: J.R. Anderson, M. Boudart (Eds.), Hydrotreating Catalysis—Science and Technology, vol. 11, Springer, Berlin/Heidelberg, 1996.
[2] R. Prins, in: G. Ertl, H. Knözinger, J. Weitkamp (Eds.), Handbook of Heterogeneous Catalysis, vol. 4, Wiley–VCH, Weinheim, 1997, pp. 1908–1928.
[3] P. Euzen, P. Raybaud, X. Krokidis, H. Toulhoat, J.-L.L. Loarer, J.-P. Jolivet, C. Froidefond, in: F. Schüth, K.S.W. Sing, J. Weitkamp (Eds.), Handbook of Porous Solids, vol. 3, Wiley–VCH, Weinheim, 2002, pp. 1591–1677.
[4] J. Ramirez, S. Fuentes, G. Díaz, M. Vrinat, M. Breysse, M. Lacroix, Appl. Catal. 52 (1989) 211.
[5] M. Breysse, J.L. Portefaix, M. Vrinat, Catal. Today 10 (1991) 489.
[6] S. Dzwigaj, C. Louis, M. Breysse, M. Cattenot, V. Bellière, C. Geantet, M. Vrinat, P. Blanchard, E. Payen, S. Inoue, H. Kudo, Y. Yoshimura, Appl. Catal. B 1265 (2002) 1.
[7] K.Y.S. Ng, E. Gulari, J. Catal. 95 (1985) 33.
[8] Q. Zhang, L. Gao, J. Guo, J. Eur. Ceram. Soc. 20 (2000) 2153.
[9] Y. Gao, S.A. Elder, Mater. Lett. 44 (2000) 228.
[10] A. Chemseddine, T. Moritz, Eur. J. Inorg. Chem. (1999) 235.
[11] C.J. Barbé, F. Arendse, P. Comte, M. Jirousek, F. Lenzmann, V. Shklover, M. Grätzel, J. Am. Ceram. Soc. 80 (1997) 3157.
[12] T. Ohno, K. Sarukawa, K. Tokieda, M. Matsumura, J. Catal. 203 (2001) 82.
[13] G. Martra, Appl. Catal. A 200 (2000) 275.
[14] A.K. Datye, G. Riegel, J.R. Bolton, M. Huang, M.R. Prairie, J. Solid State Chem. 115 (1995) 236.
[15] G. Munuera, F. Moreno, F. Gonzalez, in: J.S. Anderson, M.W. Roberts, F.S. Stone (Eds.), Reactivity of Solids, Chapman Hall, London, 1972, p. 681.
[16] G. Busca, H. Saussey, O. Saur, J.-C. Lavalley, V. Lorenzelli, Appl. Catal. 14 (1985) 245.
[17] C. Morterra, J. Chem. Soc., Faraday Trans. 1 84 (1988) 1617.
[18] J.A.R.V. Veen, Z. Phys. Chem. 162 (1988) 215.
[19] K.I. Hadjiivanov, D. Klissurski, Chem. Soc. Rev. (1996) 61.
[20] A. Travert, O.V. Manoilova, A.A. Tsyganenko, F. Maugé, J.C. Lavalley, J. Phys. Chem. B 106 (2002) 1350.
[21] U. Diebold, Surf. Sci. Rep. 48 (2003) 53.
[22] J. Ziólkowski, Surf. Sci. 209 (1989) 356.
[23] P.M. Olivier, G.W. Watson, E.T. Kelsey, S.C. Parker, J. Mater. Chem. 7 (1997) 563.
[24] T. Bredow, K. Jug, Surf. Sci. 327 (1995) 398.
[25] A. Fahmi, C. Minot, Surf. Sci. 304 (1994) 343.
[26] A. Beltrán, J.R. Sambrano, M. Calatayud, F.R. Sensato, J. Andrés, Surf. Sci. 490 (2001) 116.
[27] H. Schweiger, P. Raybaud, G. Kresse, H. Toulhoat, J. Catal. 207 (2002) 76.
[28] H. Schweiger, P. Raybaud, H. Toulhoat, J. Catal. 212 (2002) 33.
[29] P. Raybaud, M. Digne, R. Iftmie, W. Wellens, P. Euzen, H. Toulhoat, J. Catal. 201 (2001) 236.
[30] M. Digne, P. Sautet, P. Raybaud, P. Euzen, H. Toulhoat, J. Catal. 211 (2002) 1–5.
[31] J.P. Perdew, Y. Wang, Phys. Rev. B 45 (1992) 13244.
[32] G. Kresse, J. Hafner, Phys. Rev. B 47 (1993) 558.
[33] G. Kresse, J. Hafner, Phys. Rev. B 48 (1993) 13115.
[34] G. Kresse, J. Hafner, Phys. Rev. B 49 (1994) 14251.
[35] G. Kresse, J. Furthmüller, Comput. Mater. Sci. 6 (1996) 15.
[36] G. Kresse, D. Joubert, Phys. Rev. B 59 (1999) 1758.
[37] I.N. Senchenya, E. Garrone, P. Ugliengo, J. Mol. Struct. (Theochem) 368 (1996) 93.
[38] P. Ugliengo, ANHARM, A program to solve numerically the monodimensional nuclear Schrödinger equation, unpublished.
[39] G. Wulff, Z. Kristallogr. 34 (1901) 449.
[40] X.G. Wang, A. Chaka, M. Scheffler, Phys. Rev. Lett. 84 (2000) 3650.
[41] F. Schossberger, Z. Kristallogr. Kristallogeom. Kristallophys. Kristallochem. 104 (1942) 358.
[42] L. Vegard, Philos. Mag. 32 (1916) 505.
[43] M. Ramamoorthy, D. Vanderbilt, R.D. King-Smith, Phys. Rev. B 49 (1994) 16721.
[44] A. Vittadini, A. Selloni, F.P. Rotzinger, M. Grätzel, Phys. Rev. Lett. 81 (1998) 2954.
[45] L. Giordano, J. Goniakowski, J. Suzanne, Phys. Rev. Lett. 81 (1998) 1271.
[46] X. Krokidis, P. Raybaud, A.-E. Gobichon, B. Rebours, P. Euzen, H. Toulhoat, J. Phys. Chem. B 105 (2001) 5121.
[47] J.P. Beaufils, Y. Barbaux, J. Chim. Phys. 78 (1981) 347.